Alpine ice evidence of a three-fold increase in atmospheric iodine deposition since 1950 in Europe due to increasing oceanic emissions

Michel Legrand[a,1], Joseph R. McConnell[b], Susanne Preunkert[a], Monica Arienzo[b], Nathan Chellman[b], Kelly Gleason[b], Tomás Sherwen[c,d], Mat J. Evans[c,d], and Lucy J. Carpenter[c]

[a]Institut des Géosciences de l'Environnement, Université Grenoble Alpes-CNRS, 38400 Saint-Martin d'Hères, France; [b]Division of Hydrologic Sciences, Desert Research Institute, Reno, NV 89512; [c]Wolfson Atmospheric Chemistry Laboratories, Department of Chemistry, University of York, York, YO10 5DD, United Kingdom; and [d]National Centre for Atmospheric Science, University of York, York, YO10 5DD, United Kingdom

Edited by Daniel J. Jacob, Harvard University, and accepted by Editorial Board Member A. R. Ravishankara October 16, 2018 (received for review June 7, 2018)

Iodine is an important nutrient and a significant sink of tropospheric ozone, a climate-forcing gas and air pollutant. Ozone interacts with seawater iodide, leading to volatile inorganic iodine release that likely represents the largest source of atmospheric iodine. Increasing ozone concentrations since the preindustrial period imply that iodine chemistry and its associated ozone destruction is now substantially more active. However, the lack of historical observations of ozone and iodine means that such estimates rely primarily on model calculations. Here we use seasonally resolved records from an Alpine ice core to investigate 20th century changes in atmospheric iodine. After carefully considering possible postdepositional changes in the ice core record, we conclude that iodine deposition over the Alps increased by at least a factor of 3 from 1950 to the 1990s in the summer months, with smaller increases during the winter months. We reproduce these general trends using a chemical transport model and show that they are due to increased oceanic iodine emissions, coupled to a change in iodine speciation over Europe from enhanced nitrogen oxide emissions. The model underestimates the increase in iodine deposition by a factor of 2, however, which may be due to an underestimate in the 20th century ozone increase. Our results suggest that iodine's impact on the Northern Hemisphere atmosphere accelerated over the 20th century and show a coupling between anthropogenic pollution and the availability of iodine as an essential nutrient to the terrestrial biosphere.

iodine | Alpine ice core | GEOS-Chem | tropospheric ozone | trend

In addition to their role in stratospheric chemistry (1), the importance of halogens in tropospheric chemistry first emerged from the observation of sudden decreases in surface ozone in the Arctic during spring (2). More recently, the pervasive impact of halogens on tropospheric ozone over the open ocean was identified (3, 4). The majority of halogen-related surface ozone destruction is attributable to iodine chemistry, which is calculated to decrease the global tropospheric O_3 burden by ∼9% and up to 45% regionally (5–8). Iodine is also a direct major public health issue; iodine deficiency occurs in many parts of the world, with the severest effects including endemic goiter and irreversible mental retardation. Atmospheric deposition through precipitation and dry deposition is the main contributor of terrestrial iodine and thus may directly determine the prevalence of iodine deficiency disorders (9). In its last review, the World Health Organization (10) concluded that iodine deficiency remains a significant public health problem in Europe, with the populations of 11 countries, including France and Italy, and some regions of Spain, having insufficient iodine. Reconstructing the past iodine content of precipitation in the Alps is therefore of particular interest.

For several decades, the main source of iodine was considered to be oceanic emission of volatile halogenated organic compounds (CH_3I, CH_2I_2, CH_2ICl, and CH_2IBr) (11–13). More recently, laboratory studies established that hypoiodous acid (HOI) and molecular iodine (I_2) are emitted from ocean waters following the reaction of O_3 with iodide (I^-) at the air–sea interface (14). Using parameterizations of the air–sea flux of inorganic iodine, models show that this sea surface source represents around 75% of total iodine emissions (5, 15).

Inorganic iodine emissions are thus likely to have increased in response to enhancement of surface O_3 levels resulting from anthropogenic activities. However, ozone observations made before 1950 are highly uncertain (16), and, between the 1950s and the 1990s, the O_3 observational network was still relatively incomplete. Model simulations tend to underestimate the observed increase in surface ozone in this period by a factor of 2 (17).

Once emitted into the atmosphere, iodine species are rapidly photolyzed into I atoms that react with O_3 to produce IO. In addition to IO self-reactions producing higher oxides (I_2O_x), IO reacts with HO_2, forming back HOI, or reacts with NO_2 to produce $IONO_2$ (18). Model simulations indicate that, in the free troposphere, HOI is the dominant inorganic iodine (I_y) species (70%), followed by IO and $IONO_2$ (5, 15). Whereas $IONO_2$ is very water-soluble [assumed Henry's law constant (H) of ∞; ref. 19], HOI is much less soluble in water (H = >415 $M{\cdot}atm^{-1}$ at 298 K; ref. 19).

Significance

Our measurements show a tripling of iodine in Alpine ice between 1950 and 1990. A 20th century increase in global iodine emissions has been previously found from model simulations, based on laboratory studies, but, up to now, long-term iodine records exist only in polar regions. These polar records are influenced by sea ice processes, which may obscure global iodine trends. Our results suggest that the increased iodine deposition over the Alps is consistent with increased oceanic iodine emissions coupled with a change in the iodine speciation, both driven by increasing anthropogenic NO_x emissions. In turn, the recent increase of iodine emissions implies that iodine-related ozone loss in the troposphere is more active now than in the preindustrial period.

Author contributions: M.L., J.R.M., S.P., M.A., N.C., T.S., M.J.E., and L.J.C. performed research; M.L., J.R.M., S.P., M.A., N.C., K.G., T.S., M.J.E., and L.J.C. analyzed data; and M.L., J.R.M., T.S., M.J.E., and L.J.C. wrote the paper.

The authors declare no conflict of interest.

This article is a PNAS Direct Submission. D.J.J. is a guest editor invited by the Editorial Board.

[1]To whom correspondence should be addressed. Email: michel.legrand@univ-grenoble-alpes.fr.

This article contains supporting information online at www.pnas.org/lookup/suppl/doi:10.1073/pnas.1809867115/-/DCSupplemental.

Published online November 12, 2018.

While laboratory and modeling studies have indicated that the dominant source of atmospheric iodine is the emission of HOI and I_2 from the surface ocean following ozone deposition (14), the strength of this source and its past variability remain poorly quantified. Uncertainties relate to (*i*) ozone changes over the ocean since preindustrial (PI) times, (*ii*) the concentration of iodide in the surface ocean, and (*iii*) understanding and parameterizations of the HOI and I_2 flux, all of which suffer from a lack of observational constraints. Finally, there are far greater uncertainties in iodine chemistry than bromine, in particular, rates and products of heterogeneous reactions on aerosol and the photolysis of higher oxide iodine species (18).

Chemical records of species trapped in snow deposited on cold glaciers provide a unique and powerful way to reconstruct past atmospheric chemistry changes (20). Cold low-latitude glaciers are nearly nonexistent, however, and, to date, ice core iodine records have been developed only from polar ice cores extracted where the halogen chemistry is dominated by local sea ice-related photochemical and biological mechanisms that produce both bromine and iodine (21, 22). Due to low net surface snow accumulation rates, polar ice cores also may suffer from significant remobilization and loss after snow deposition of volatile iodine species such as HOI. It has also been shown that iodine can escape from firn, a porous material, after core extraction (*SI Appendix*), limiting the study of recent snow layers. Alternatively, ice core records from low-latitude or northern midlatitude glaciers potentially offer much better constraints of historical changes in oceanic inorganic iodine emission/deposition, since they are predominantly affected by the globally dominant sea surface emission rather than local sea ice processes and, because of high snow accumulation rates, may be less affected by postdepositional volatilization of iodine. Here we show ice core data from the Col du Dome (CDD) site, an area characterized by very high net snow accumulation rate ranging from 0.50 m to ∼2.40 m water equivalent per year ($mwe{\cdot}y^{-1}$) (23) such that the firn–ice transition (i.e., density of 0.83 $g{\cdot}cm^{-3}$) corresponds to an age of just 15 y to 18 y before the year of collection. For comparison, the firn–ice transition at the Summit site in central Greenland where the snow accumulation rate is of 0.22 $mwe{\cdot}y^{-1}$ (*SI Appendix*) corresponds to an age of 220 y.

We developed a seasonally resolved, northern midlatitude ice core record of iodine from 1890 to 2000 from ice cores extracted from a cold, high elevation (4,250 m) site at CDD in the French Alps. We used this record, as well as simulations using the GEOS-Chem chemistry transport model, to investigate past atmospheric iodine concentrations and changes in atmospheric speciation and deposition over Europe. Because of the volatility of iodine, we also considered the potential impacts of postdepositional losses from the snow on the ice core iodine record.

Results and Discussion

Mean summer and winter iodine concentrations measured in the CDD ice from 1890 to 2000 during the 20th century (Fig. 1*A*) show substantial increases, especially in the summer months. The summer iodine record is characterized by two distinct time periods, with relatively constant summer concentrations from 1890 to 1950 (0.025 ± 0.01 $ng{\cdot}g^{-1}$), followed by a steady increase after 1950, with concentrations reaching 0.16 ± 0.05 $ng{\cdot}g^{-1}$ after 1995. In contrast, the long-term winter trend is less pronounced, with concentrations close to 0.02 ± 0.01 $ng{\cdot}g^{-1}$ from 1890 to 1950, 0.03 ± 0.01 $ng{\cdot}g^{-1}$ between 1950 and 1970, and 0.05 ± 0.02 $ng{\cdot}g^{-1}$ between 1970 and 1995.

Due to an accumulation surplus by drifting snow at the drill site located at the saddle and wind snow erosion upstream of the drill site, a decrease with depth of the net snow accumulation was observed in the CDD ice cores (*SI Appendix*, Fig. S3*C*). Such changes with depth may possibly induce a nonatmospheric effect in the iodine ice record. Indeed, consistent with the high volatility of some of the iodine species (HOI), iodine concentrations in ice were found to be dependent on the annual snowfall rate, particularly at sites with low snowfall rates (*SI Appendix*). To distinguish changes in atmospheric iodine levels through time from potential effects of changing snow deposition rate, we examined the CDD ice record of iodine for different ranges of annual ice layer thickness (ILT). This careful examination of the CDD ice record covering the years 1890–1950 suggests a small postdepositional effect on iodine concentrations (*SI Appendix*). Nevertheless, we estimate that, between 1890 and 1950, the summer iodine deposition in the ice increased by 0.01 $ng{\cdot}g^{-1}$ to 0.02 $ng{\cdot}g^{-1}$ from early 1890 to around 1905. This was followed by a decrease of 0.01 $ng{\cdot}g^{-1}$ to 0.02 $ng{\cdot}g^{-1}$ from the early to late 1930s (*SI Appendix*, Fig. S4*B*). Although coal burning in Europe and the practice of kelp burning used by the iodine industry along the west coast of Europe (*SI Appendix*) emit iodine into the atmosphere, these two sources are significantly weaker than oceanic emissions, and we estimate that their contribution to iodine concentrations in the CDD ice are limited to 0.02 $ng{\cdot}g^{-1}$ (*SI Appendix*). The small decrease of iodine between 1930 and 1945 may be related to the reduction of these two emission sources during World War II.

Annual ILT in the CDD record increased in the late 20th century, from 0.5 mwe between 1930 and 1950 to 1.5 mwe between 1965 and 1980, potentially contributing to the concurrent increases in iodine concentrations. To accurately quantify changes in atmospheric iodine after 1950, summer iodine levels were separated into two sets based on their respective annual thickness (ILT < 1.5 mwe and ILT > 1.5 mwe) (*SI Appendix*, Fig. S4*A*). From this analysis, we conclude (*SI Appendix*) that, even though part of the observed trend may be attributed to changing snow deposition conditions, the CDD record suggests an increasing trend in summer atmospheric iodine of at least a factor of 3 from 1950 to 1995. In contrast, wintertime iodine levels increased by only a factor of 2 over the same period (Fig. 1*A*). Whereas kelp burning ceased after 1950, before 1965, coal consumption in Western Europe remained similar to that in 1930 and dropped in the 1990s (*SI Appendix*). Since the iodine content is 4 times lower in petroleum than in coal, it can be concluded that fossil fuel burning did not significantly contribute to the observed increase of iodine in the CDD summer layers between 1950 and 2000. The iodine trends seen in the Alps may therefore mainly reflect change in iodine emissions from oceanic regions located offshore Western Europe.

We simulate global tropospheric iodine chemistry using the GEOS-Chem chemical transport model (15) (*Materials and Methods*). This considers both organic and inorganic iodine emissions, photochemical and heterogeneous iodine chemistry, and deposition. GEOS-Chem simulations show that Western Europe (notably the Mediterranean) represents a region where oceanic iodine emissions are particularly strong and the change from PI to present day (PD) is expected to be very significant (*SI Appendix*, Fig. S6). Overlaid on the summer and winter time series of iodine concentrations in Fig. 1*A* are model simulations of summer and winter iodine deposition for the CDD grid box run with emissions appropriate for the PI era (1850), 1950, 1980, 1995, and for the PD (2005) (24) (*Materials and Methods*). It is not possible to directly compare modeled atmospheric iodine deposition rates with the concentration of iodine within the CDD ice because of uncertainties associated with annual precipitation, snow accumulation in complex mountain glaciers, and the relatively coarse resolution of the model (250 km × 200 km). Nevertheless, we consider that the long-term trends in iodine concentration at CDD should be associated with long-term trends in iodine deposition and are mutually influenced by changes in iodine emissions as well as atmospheric iodine concentrations and speciation.

If we assume that all of the deposited iodine (predominantly HOI, $IONO_2$, iodine aerosol, HI, and IO) remains in the ice, the model shows an increase of 70% in the summertime from the PI to the PD (0.79×10^{-13} $kg{\cdot}m^2{\cdot}s^{-1}$ to 1.33×10^{-13} $kg{\cdot}m^2{\cdot}s^{-1}$).

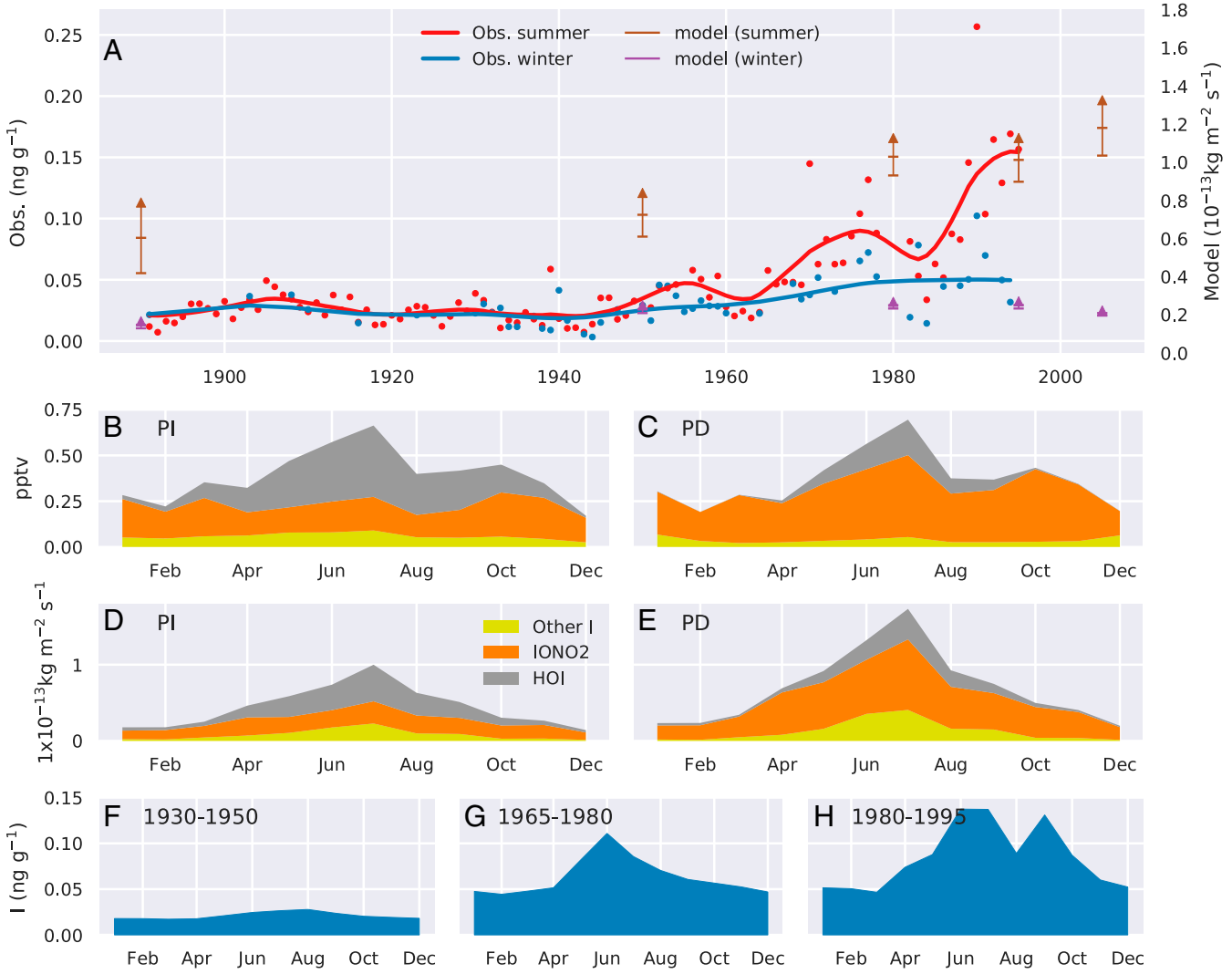

Fig. 1. (*A*) Time series of iodine in Col du Dome ice core in summer (red) and winter (blue). Dots are yearly values; solid lines are the first component of a single spectra analysis with a 7-y time window (summer) and robust spline (winter). Vertical bars show the modeled mean deposition for summer (brown) and winter (purple) for 1850 (shown at 1890), 1950, 1980, 1995, and 2005. The dashes and arrow on the bars show the deposition of inorganic iodine minus HOI (lower dash) and minus half of HOI deposition (middle dash), and the total (top arrow). (*B* and *C*) Modeled seasonality of surface iodine species mixing ratio in 1850 (PI) and 2005 (PD); other iodine is composed of HI, I_2, I_xO_y, IBr, ICl, IONO, and aerosol phase iodine. (*D* and *E*) Modeled seasonality of iodine species deposition. (*F–H*) Seasonal cycle of iodine measured in the CDD ice cores averaged for three time periods: 1930–1950, 1965–1980, and 1980–1995. Outlier values in winter 1994/1995 were not considered, as well as values observed in the 1948 summer layers (*SI Appendix*). Data obtained in firn layers were also not considered (*SI Appendix*).

However, given the low Henry's law constant of HOI, it may revolatilize from the snow after deposition. If we assume that half the deposited HOI undergoes postdepositional release and so only include half the simulated HOI deposition in the total calculated deposition, we calculate a larger increase of approximately a factor of 2 in net deposited iodine from the PI to the PD (0.60×10^{-13} kg·m^2·s^{-1} to 1.18×10^{-13} kg·m^2·s^{-1}). This increases further to a factor of 2.5 (0.42×10^{-13} kg·m^2·s^{-1} to 1.04×10^{-13} kg·m^2·s^{-1}) if all of the deposited HOI is revolatilized. It is notable that, even with the imposed upper limit of postdepositional release of HOI, the model simulates a lower increase in summertime deposition over the 20th century than observed (Fig. 1*A*).

This increase from the PI to the PD iodine deposition could be driven by increases in iodine emissions, changes in atmospheric iodine speciation and hence lifetime against deposition, or changes in precipitation. Long-term variations of precipitation in the Alps do not reveal significant trends over the 20th century (25). The modeled annual oceanic iodine emissions in the nearby Atlantic and Mediterranean regions (defined by the region shown in Fig. 2), however, more than double (2.2) (from 18.7 Gg·y^{-1} to 40.1 Gg·y^{-1}) between the PI and PD (Fig. 2), reflecting increases in the simulated O_3 concentrations; the tropospheric ozone burden increases from 235 Tg (O_3) in the PI to 321 Tg (O_3) in the PD, generally consistent with other models (26). The simulated tropospheric ozone increase from the PI to the PD, which mainly results from increased anthropogenic NO_x emissions, has been shown to be reduced by ~25% when enhanced ozone destruction due to increased atmospheric halogen concentrations, including iodine, is accounted for (7).

To estimate the impact of increasing ocean emissions alone on iodine deposition at CDD, we ran the model for the PD using archived PI I_2 and HOI emissions (see *Materials and Methods* and *SI Appendix*, Fig. S7). We find that PD annual mean iodine deposition almost doubles (1.85 regardless of HOI volatilization assumption) using the PD iodine emissions rather than the PI iodine emissions. Fig. 1 *B* and *C* shows that, despite this increased ocean source, the model calculates a marginally lower total atmospheric inorganic iodine (I_y) concentrations at the site in

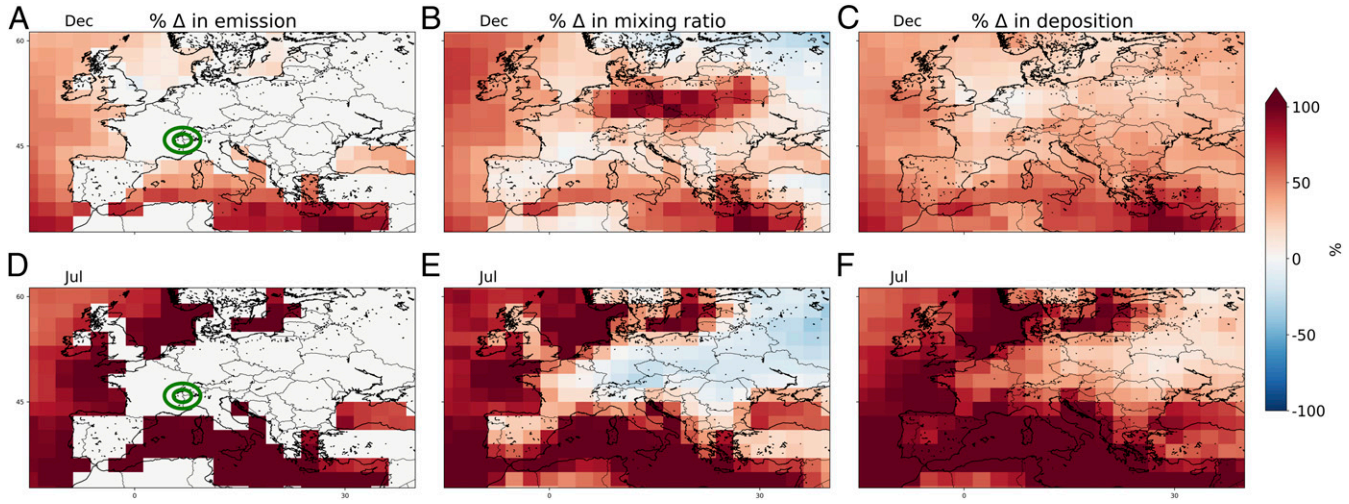

Fig. 2. Modeled percentage change between PI (1850) and PD (2005) changes in December and July (*A* and *D*) iodine emissions, (*B* and *E*) surface inorganic iodine concentrations, and (*C* and *F*) inorganic iodine deposition. Concentric green circles give the location of CDD.

the PD [annual mean of 0.37 part per trillion by volume (pptv)] than the PI (0.39 pptv). The reason for the decreased atmospheric abundance is a change in iodine speciation from being predominantly HOI in the PI to the more water-soluble $IONO_2$ in the PD (Fig. 1*B*). As $IONO_2$ is more soluble, this decreases the atmospheric lifetime of I_y and so leads to lower I_y concentrations over much of Europe (Fig. 2 *B* and *E*). The large change in European anthropogenic NO_x emissions after 1950 (24), as clearly reflected in the increasing trends of nitrate in CDD ice (*SI Appendix*, Fig. S3*B*), is responsible for this increased fraction of iodine as $IONO_2$ rather than HOI. This shortening of the lifetime also leads to increased deposition at CDD in the PD because of the higher solubility of $IONO_2$ (Figs. 1 *D* and *E* and 2 *C* and *F*). At CDD, these two opposing factors approximately cancel (the change in atmospheric composition reduces the deposition at CDD by ∼3%), such that oceanic emission increases are the predominant driver of the summertime increases in iodine deposition at CDD. These deposition changes are coupled in complex ways to a change in iodine speciation over Europe due to growing nitrogen oxide emissions. At other sites, however, the modeled change in composition has a much larger influence. Thus, we suggest that oceanic emission increases are the main driver of the summertime increases in iodine deposition at CDD, although these are coupled in complex ways to a change in iodine speciation over Europe due to growing nitrogen oxide emissions. Other locations will respond to these changes in different ways (Fig. 2). Significant uncertainties remain in atmospheric iodine photokinetics (15), which may influence this partitioning.

The modeled seasonal cycles in iodine deposition (Fig. 1 *D* and *E*) in the PI and PD show very similar features to the observed seasonal cycles in the ice core (Fig. 1 *F*–*H*), which also are characterized by a summer maximum that has increased in amplitude over the 20th century: from 1.3 (summer/winter iodine concentration) between 1930 and 1950 to ∼1.9 between 1980 and 1995. Our model results show that the seasonal cycle is due to (*i*) elevated summertime iodine emissions due to higher ozone concentrations in the summer, (*ii*) a shorter atmospheric iodine lifetime in the winter months due to $IONO_2$ comprising a higher proportion of total I_y in winter, which has become more pronounced in the PD, and (*iii*) more precipitation in the summer months compared with winter.

The model's underestimate of the increase in the iodine deposition at CDD (1.7 to 2.5, depending on the HOI assumption compared with a measured change of 3) between the PI and PD may be due to an underestimate in the PI to PD change of surface O_3. This has been discussed previously, both based on very early (19th century) measurements (27) and more recent (1960 to PD) data (17); however, more recent analysis suggests sampling bias may explain some of the differences (28). A comparison between the 19th century O_3 observations and the model (*SI Appendix*, Fig. S8) shows that the model overestimates these observations by roughly 50%. A model simulation that reduces the PI ocean iodine flux by 50%, consistent with a model overestimate of surface ozone concentration in the PI by a factor of 2, leads to a lower PI iodine deposition and thus a larger fractional change between the PI and PD. This gives an increase in the summer iodine deposition in the range 2.6 to 3.6 (depending on assumptions regarding HOI volatilization), which would make the model consistent with observations.

In Fig. 2, we show modeled changes in iodine emissions, surface atmospheric iodine mixing ratio, and deposition of total atmospheric iodine between the PI and PD over Europe for December and July. Ocean iodine emissions increase significantly between the PI and the PD, and the anthropogenically driven spring/summer maximum in O_3 in the region leads to a larger increase in ocean emissions in the summer months than in the winter (Fig. 2 *A* and *D*). Close to the coast, surface I_y concentrations increase to reflect this increase in the source (Fig. 2 *B* and *E*). However, atmospheric iodine mixing ratios over land have increased significantly less than emissions and, in many regions, have decreased because of enhanced NO_2 concentrations that promote formation of $IONO_2$ and shorten the depositional lifetime of atmospheric iodine over the land. However, the shorter depositional lifetime results in more efficient deposition of the available I_y, and so overall deposition fluxes increase over the Alps consistent with the observations. In some locations (northern Europe in the winter, Ukraine in the summer), deposition of I_y has reduced from the PI to the PD due to this change in I_y speciation from HOI to $IONO_2$.

This study of an 1890–2000 ice core record of iodine extracted for the first time from a northern midlatitude glacier reveals an increase in iodine concentrations from the early 1950s to the beginning of the mid-1990s. After carefully considering possible biases induced by postdepositional losses of these volatile species from the snow and taking advantage of the very high snow accumulation rate at this Alpine site, we find that, whereas only small changes were detected before 1950, potentially partly due to changes in kelp burning and coal burning emissions, atmospheric iodine deposition over the Alps (and potentially more widely) increased from 1950 to 1995 by about a factor of 2 in winter and a

factor of at least 3 in summer. GEOS-Chem simulations show that Western Europe represents a unique region where oceanic iodine emissions are particularly strong and the change from PI to PD is expected to be very significant (*SI Appendix*, Fig. S6). We attribute the marked increase in iodine deposition over the 20th century to inorganic iodine emissions from the Atlantic Ocean and Mediterranean Sea that have grown in response to enhanced surface ozone concentrations arising from increased NO_x emissions, alongside an enhanced contribution of the very water-soluble $IONO_2$ species following growing anthropogenic NO_x emissions, that leads to more efficient iodine scavenging into the snow/ice. We note that the model PD deposition is 170% of the PI deposition if HOI is considered involatile and 250% if it is not, both less than observations in the ice core. Surface ozone concentrations in the PI significantly lower than those modeled would reconcile the model and measured changes in iodine deposition. Overall, this study identifies and attributes an increase in iodine deposition over Western Europe, including the Alps where iodine deficiency was first recognized, likely leading to enhanced iodine content in water, soils, and vegetation during the latter half of the 20th century.

Materials and Methods

Site, Ice Core Dating, and Methods. Chemical measurements were made on two ice cores extracted at the CDD site (45°50′N, 6°50′E, 4,250 m above sea level) located in the French Alps. The first core (denoted C10, 126 m long) was drilled in 1994, and the second core (denoted CDM, 140 m long), extracted less than 20 m away from the C10, was drilled in 2012. As discussed in *SI Appendix*, iodine can escape from the firn (a porous material with a density of <0.83 g·cm^{-3}) after core extraction either during storage or melting of samples before analysis. Therefore, we restricted iodine analysis to parts of the cores with a density of >0.70 g·cm^{-3} (i.e., ice and dense firn). The CDD site area is characterized by a very high net snow accumulation rate ranging from 0.50 mwe·y^{-1} to ∼2.40 mwe·y^{-1} (23) so the firn–ice transition (i.e., density of 0.83 g·cm^{-3}) corresponds to an age of just 15 y to 18 y before the year of collection. The quality of data obtained in the dense firn layers (density ranging from 0.70 g·cm^{-3} to 0.83 g·cm^{-3}) is discussed in *SI Appendix*.

The entire C10 core was investigated previously by subsampling pieces of firn and ice with subsequent analysis by ion chromatography (IC) at the Institut des Géosciences de l'Environnement, permitting investigations of long-term trends of sulfate (29), nitrate (30), and ammonium (31). In this study, the dense firn/ice part of the C10 core (i.e., from 42.9 m to 125.7 m depth) was analyzed using a continuous analytical system at the Desert Research Institute (DRI) Ultra Trace Chemistry Laboratory. To extend the time period covered by dense firn/ice (up to 1985 at 43 m depth in the C10 core) to more recent years, the upper ice section of the CDM core (from 45.4 m to 86.7 m depth) covering the 1979–1999 time period also was analyzed using the DRI continuous system.

Longitudinal samples of ice core (cross-sectional area of 3.3 cm × 3.3 cm) were melted sequentially, with the meltwater stream split into three regions. Iodine and sulfur were measured in the meltwater from the innermost ring (10% of the sample cross-section) by inductively coupled plasma–mass spectrometers [Thermo Scientific Element 2 high resolution with a concentric Teflon nebulizer (electrospray ionization)] (32). Elemental measurements were made on the ultraclean sample stream, with ultrapure nitric acid added immediately after the melter plate to yield an acid concentration of ∼1%. Meltwater from the middle ring was used for traditional continuous flow measurements of nitrate and ammonium (33, 34). Effective depth resolution differs between the instruments in the analytical system and operating parameters, but, in this study, was estimated to be ∼ 0.02 m for I, with all measurements exactly coregistered in depth. The detection limit (defined as 3 times the SD of the blank) was 0.003 ng·g^{-1} for I. Among species that were coanalyzed, we used a few ancillary data on bromine and lead concentrations for which detection limits are of 0.06 and 0.0006 ng·g^{-1}, respectively. Noncrustal or excess lead (Pb_{ex}) was calculated from measured total lead following standard procedures (35) using a Ce/Pb crustal ratio of 83/19 (36). As shown in *SI Appendix*, Fig. S1, the agreement between IC and continuous measurements on the C10 core was excellent for ammonium, nitrate, and sulfate.

Dating of the CDD cores was established by counting annual layers along the ammonium profile (23) characterized in Alpine snow by midwinter concentration minima (*SI Appendix*, Fig. S1). On this basis and using reference horizons (the 1963 tritium or ^{137}Cs bomb peak; the dust horizons of 1977, 1947, and 1936), the date of 1920 ± 5 y was attributed to the 118-m depth (i.e., 90 mwe) in the C10 core down (23). Further investigations conducted on fluoride levels showed a well-marked increase from 0.3 ng·g^{-1} in 1930 to 1.4 ng·g^{-1} in 1940, coinciding well with historical emissions related to development of the aluminum industry in Western Europe before the Second World War (37). Therefore, when reexamining the dating in light of new information provided by the Pb profile (see below), we did not change the dating back to 1935. We extended the dating to 1890 by using the distinct 1890 increases in heavy metal (noncrustal lead, cadmium, thallium) concentrations associated with widespread coal burning during the early Industrial Revolution. Such increases are clear in well-dated Greenland ice cores (38). The 1890 tie point was used as a constraint to extend annual layer counting to 1890. Before 1890, our continuous measurements indicated that no winter snow was preserved, consistent with understanding of upstream deposition processes. From that, we obtained an ice core CDD record covering the time period from 1890 through 1982 in the C10 core and from 1982 to 1999 in the CDM core.

GEOS-Chem Model Description and Simulations. The simulations of tropospheric iodine chemistry use the GEOS-Chem chemical transport model (www.geos-chem.org/, v10-01), updated with the halogen chemistry, emissions, and deposition (15). Inorganic iodine emissions are based on the ozone ocean–iodide relationship from Carpenter et al. (14), with ocean iodide concentrations calculated from the parameterizations of MacDonald et al. (39). Organic iodine emissions are from Ordóñez et al. (40). Each simulation was run for 2 y (2004–2006), driven by meteorology from the NASA Goddard Modeling and Assimilation Office GEOS-5 archive and discarding the first year as a spin-up. The simulations for the PD (2005) and PI (1850) were run at 2° × 2.5° horizontal resolution, with the latter reducing methane concentration to 700 pptv, removing the anthropogenic contribution to bromine and chlorine emissions following Sherwen et al. (7), using historical Atmospheric Chemistry and Climate Model Intercomparison Project (ACCMIP) anthropogenic emissions (24). The simulations for 1950, 1980, and 1995 were run at a horizontal resolution of 4° × 5° and used the ACCMIP anthropogenic and biomass burning emissions (24) and fixed surface methane concentrations based on observations for a given year (41). Other emissions fluxes are the same in all simulations, including biogenic VOCs (42), soil NO_x (43), lightning (44), and stratospheric sources (44). Two additional sensitivity simulations were performed at a resolution of 4° × 5°: (*i*) PD simulation (2005) where the online (driven by the ozone concentration) HOI and I_2 emissions where replaced by monthly mean emissions fluxes from the 4° × 5° resolution PI simulation, and (*ii*) PI (1850) but with the online parameterization of HOI and I_2 emissions (14) provided with the half the modeled value of surface ozone at any time step to simulate the impact of potentially lower O_3 concentrations than are simulated (17, 27). When evaluating the impact of postdepositional HOI loss, the same simulation is used, but the diagnosed total I deposition only includes half or none of the HOI deposition.

ACKNOWLEDGMENTS. R. Kreidberg at DRI provided editorial advice. We thank Eric Wolff for very useful comments on the ice core data. Thanks go to Adrien Gilbert, who extracted ice flow parameters from the model he recently developed for the Mont Blanc glacier. The drilling operations to extract the C10 and CDM ice cores at Col du Dome (French Alps) were supported by the European Community via Contract ENV4-CT97 and the Region Rhône-Alpes. The Les Enveloppes Fluides et l'Environnement- Chimie Atmosphérique (CNRS) program entitled "Evolution séculaire de la charge et composition de l'aérosol organique au dessus de l'Europe" provided funding for analysis in France, with the support of Agence de l'Environnement et de la Maîtrise de l'Energie. L.J.C., M.J.E., and T.S. acknowledge support from Natural Environment Research Council through Grants NE/L01291X/1 and NE/N009983/1 and computer time on the York Advanced Research Computing Cluster. We acknowledge Emissions of Atmospheric Compounds and Compilation of Ancillary Data for use of ACCMIP emissions data.

1. Molina MJ, Rowland FS (1974) Stratospheric sink for chlorofluoromethanes: Chlorine atom-catalysed destruction of ozone. *Nature* 249:810–812.
2. Bottenheim JW, Gallant AG, Brice KA (1986) Measurements of NO_y species and O_3 at 82° N latitude. *Geophys Res Lett* 13:113–116.
3. Read KA, et al. (2008) Extensive halogen-mediated ozone destruction over the tropical Atlantic Ocean. *Nature* 453:1232–1235.
4. Dix B, et al. (2013) Detection of iodine monoxide in the tropical free troposphere. *Proc Natl Acad Sci USA* 110:2035–2040.
5. Saiz-Lopez A, et al. (2014) Iodine chemistry in the troposphere and its effect on ozone. *Atmos Chem Phys* 14:19985–20044.
6. Sarwar G, et al. (2015) Impact of enhanced ozone deposition and halogen chemistry on tropospheric ozone over the Northern Hemisphere. *Environ Sci Technol* 49:9203–9211.
7. Sherwen T, Evans MJ, Carpenter LJ, Schmidt JA, Mickley LJ (2017) Halogen chemistry reduces tropospheric O_3 radiative forcing. *Atmos Chem Phys* 17:1557–1569.
8. Sherwen T, et al. (2016) Global impacts of tropospheric halogens (Cl, Br, I) on oxidants and composition in GEOS-Chem. *Atmos Chem Phys* 16:12239–12271.

9. Fuge R, Johnson CC (1986) The geochemistry of iodine–A review. *Environ Geochem Health* 8:31–54.
10. Andersson M, de Benoist B, Darnton-Hill I, Delange F, eds (2007) *Iodine Deficiency in Europe. A Continuing Public Health Problem* (World Health Org, Geneva).
11. Liss PS, Slater PG (1974) Flux of gases across air-sea interface. *Nature* 247:181–184.
12. Davis D, et al. (1996) Potential impact of iodine on tropospheric levels of ozone and other critical oxidants. *J Geophys Res Atmos* 101:2135–2147.
13. Jones CE, et al. (2010) Quantifying the contribution of marine organic gases to atmospheric iodine. *Geophys Res Lett* 37:L18804.
14. Carpenter LJ, et al. (2013) Atmospheric iodine levels influenced by sea surface emissions of inorganic iodine. *Nat Geosci* 6:108–111.
15. Sherwen T, et al. (2016) Iodine's impact on tropospheric oxidants: A global model study in GEOS-Chem. *Atmos Chem Phys* 16:1161–1186.
16. Cooper OR, et al. (2014) Global distribution and trends of tropospheric ozone: An observation-based review. *Elem Sci Anth* 2:000029.
17. Parrish DD, et al. (2014) Long-term changes in lower tropospheric baseline ozone concentrations: Comparing chemistry-climate models and observations at northern midlatitudes. *J Geophys Res Atmos* 119:5719–5736.
18. Saiz-Lopez A, et al. (2012) Atmospheric chemistry of iodine. *Chem Rev* 112:1773–1804.
19. Sander R (2015) Compilation of Henry's law constants (version 4.0) for water as solvent. *Atmos Chem Phys* 15:4399–4981.
20. Legrand M, Mayewski P (1997) Glaciochemistry of polar ice cores: A review. *Rev Geophys* 35:219–243.
21. Saiz-Lopez A, et al. (2007) Boundary layer halogens in coastal Antarctica. *Science* 317: 348–351.
22. Cuevas CA, et al. (2018) Rapid increase in atmospheric iodine levels in the North Atlantic since the mid-20th century. *Nat Commun* 9:1452.
23. Preunkert S, Wagenbach D, Legrand M, Vincent C (2000) Col du Dôme (Mt Blanc Massif, French Alps) suitability for ice-core studies in relation with past atmospheric chemistry over Europe. *Tellus B Chem Phys Meterol* 52:993–1012.
24. Lamarque J-F, et al. (2010) Historical (1850–2000) gridded anthropogenic and biomass burning emissions of reactive gases and aerosols: Methodology and application. *Atmos Chem Phys* 10:7017–7039.
25. Masson D, Frei C (2016) Long-term variations and trends of mesoscale precipitation in the Alps: Recalculation and update for 1901–2008. *Int J Climatol* 36:492–500.
26. Young PJ, et al. (2013) Pre-industrial to end 21st century projections of tropospheric ozone from the Atmospheric Chemistry and Climate Model Intercomparison Project (ACCMIP). *Atmos Chem Phys* 13:2063–2090.
27. Mickley LJ, Jacob DJ, Rind D (2001) Uncertainty in preindustrial abundance of tropospheric ozone: Implications for radiative forcing calculations. *J Geophys Res Atmos* 106:3389–3399.
28. Lin M, Horowitz L, Payton R, Fiore A, Tonnesen G (2017) US surface ozone trends and extremes from 1980 to 2014: Quantifying the roles of rising Asian emissions, domestic controls, wildfires, and climate. *Atmos Chem Phys* 17:2943–2970.
29. Preunkert S, Legrand M, Wagenbach D (2001) Sulfate trends in a Col du Dome (French Alps) ice core: A record of anthropogenic sulfate levels in the European midtroposphere over the twentieth century. *J Geophys Res Atmos* 106:31991–32004.
30. Preunkert S, Wagenbach D, Legrand M (2003) A seasonally resolved alpine ice core record of nitrate: Comparison with anthropogenic inventories and estimation of preindustrial emissions of NO in Europe. *J Geophys Res Atmos* 108:4681.
31. Fagerli H, et al. (2007) Modeling historical long-term trends of sulfate, ammonium, and elemental carbon over Europe: A comparison with ice core records in the Alps. *J Geophys Res Atmos* 112:D23S13.
32. Maselli OJ, et al. (2017) Sea ice and pollution-modulated changes in Greenland ice core methanesulfonate and bromine. *Clim Past* 13:39–59.
33. Kaufmann PR, et al. (2008) An improved continuous flow analysis system for high-resolution field measurements on ice cores. *Environ Sci Technol* 42:8044–8050.
34. Pasteris D, McConnell JR, Edwards R, Isaksson E, Albert MR (2014) Acidity decline in Antarctic ice cores during the Little Ice Age linked to changes in atmospheric nitrate and sea salt concentrations. *J Geophys Res Atmos* 119:5640–5652.
35. McConnell JR, et al. (2014) Antarctic-wide array of high-resolution ice core records reveals pervasive lead pollution began in 1889 and persists today. *Sci Rep* 4:5848.
36. Bowen H (1966) *Trace Elements in Biochemistry* (Academic, New York).
37. Preunkert S, Legrand M, Wagenbach D (2001) Causes of enhanced fluoride levels in Alpine ice cores over the last 75 years: Implications for the atmospheric fluoride budget. *J Geophys Res Atmos* 106:12619–12632.
38. McConnell JR, Edwards R (2008) Coal burning leaves toxic heavy metal legacy in the Arctic. *Proc Natl Acad Sci USA* 105:12140–12144.
39. MacDonald SM, et al. (2014) A laboratory characterisation of inorganic iodine emissions from the sea surface: Dependence on oceanic variables and parameterisation for global modelling. *Atmos Chem Phys* 14:5841–5852.
40. Ordóñez C, et al. (2012) Bromine and iodine chemistry in a global chemistry-climate model: Description and evaluation of very short-lived oceanic sources. *Atmos Chem Phys* 12:1423–1447.
41. Meinshausen M, et al. (2017) Historical greenhouse gas concentrations for climate modelling (CMIP6). *Geosci Model Dev* 10:2057–2116.
42. Guenther AB, et al. (2012) The Model of Emissions of Gases and Aerosols from Nature version 2.1 (MEGAN2.1): An extended and updated framework for modeling biogenic emissions. *Geosci Model Dev* 5:1471–1492.
43. Hudman RC, et al. (2012) Steps towards a mechanistic model of global soil nitric oxide emissions: Implementation and space based-constraints. *Atmos Chem Phys* 12: 7779–7795.
44. Murray LT, Jacob DJ, Logan JA, Hudman RC, Koshak WJ (2012) Optimized regional and interannual variability of lightning in a global chemical transport model constrained by LIS/OTD satellite data. *J Geophys Res Atmos* 117:D20307.